Article

All-Evaporated, All-Inorganic CsPbI$_3$ Perovskite-Based Devices for Broad-Band Photodetector and Solar Cell Applications

Maria Isabel Pintor Monroy,* Iakov Goldberg, Karim Elkhouly, Epimitheas Georgitzikis,
Lotte Clinckemalie, Guillaume Croes, Nirav Annavarapu, Weiming Qiu, Elke Debroye, Yinghuan Kuang,
Maarten B. J. Roeffaers, Johan Hofkens, Robert Gehlhaar, and Jan Genoe

Read Online

ACCESS | Metrics & More | Article Recommendations

ABSTRACT: Following the rapid increase of organic metal halide perovskites toward commercial application in thin-film solar cells, inorganic alternatives attracted great interest with their potential of longer device lifetime due to the stability improvement under increased temperatures and moisture ingress. Among them, cesium lead iodide (CsPbI$_3$) has gained significant attention due to similar electronic and optical properties to methylammonium lead iodide (MAPbI$_3$), with a band gap of 1.7 eV, high absorption coefficient, and large diffusion length, while also offering the advantage of being completely inorganic, providing a higher thermal stability and preventing material degradation. On a device level, however, it seems also essential to replace organic transport layers by inorganic counterparts to further prevent degradation. In addition, devices are mostly fabricated by spin coating, limiting their reproducibility and scalability; in this case, exploring all-evaporated devices allows us to improve the quality of the layers and to increase their reproducibility. In this work, we focus on the deposition of CsPbI$_3$ by CsI and PbI$_2$ co-evaporation. We fabricate devices with an all-inorganic, all-evaporated structure, employing NiO and TiO$_2$ as transport layers, and evaluate these devices for both photodetector and solar cell applications. As a photodetector, low leakage current, high external quantum efficiency (EQE) and detectivity, and fast rise and decay times were obtained, while as a solar cell, acceptable efficiencies were achieved. These all-inorganic, all-evaporated devices represent one step forward toward higher stability and reproducibility while enabling large area compatibility and easier integration with other circuitry and, in future, the possible commercialization of perovskite-based technology.

KEYWORDS: perovskite, inorganic, evaporated, photodetector, solar cell

1. INTRODUCTION

In recent years, the discovery and further emergence of methylammonium lead halide perovskites (MAPbX$_3$ where X = I, Br, Cl) as an active layer for solar cells have pushed not only their use in the energy sector but also helped uncover a wide range of applications: photodetectors, light emitting diodes (LEDs), lasers, and radiation detectors.[1−4] Their high absorption coefficient, large diffusion length, and optimal band gap make them excellent substitutes or counterparts for silicon solar cells,[5,6] leading to thinner active layers, and reducing the process temperature and cost.[7,8] The further development of MAPbI$_3$-based devices has made them attractive for visible-light broad-band photodetectors in imagers: the reduced thickness of the active layer decreases the cross talk between adjacent pixels while high responsivities can be achieved, and the band gap larger than that of silicon reduces the unwanted response to infrared light.[1,9−11] However, MAPbI$_3$ devices can degrade over time, in the presence of moisture or at higher
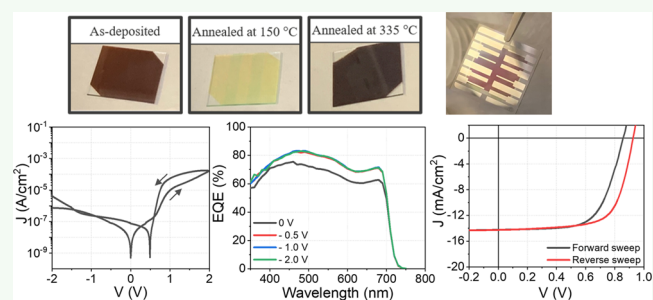
temperatures, which represents a big challenge in the scientific community.[5,12]

In recent years, cesium lead iodide perovskites (CsPbI$_3$) have been gaining more attention, as an inorganic counterpart of MAPbI$_3$, for both photodetectors and solar cell applications.[3,13,14] CsPbI$_3$ exhibits a direct band gap close to that of MAPbI$_3$ (E_g = 1.7 eV) and similar electronic and optical properties—large absorption coefficient over the whole visible range (300−720 nm), high mobilities, and long diffusion lengths—while offering the advantages of being all-inorganic: slower degradation at high temperatures or in the presence of
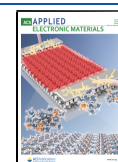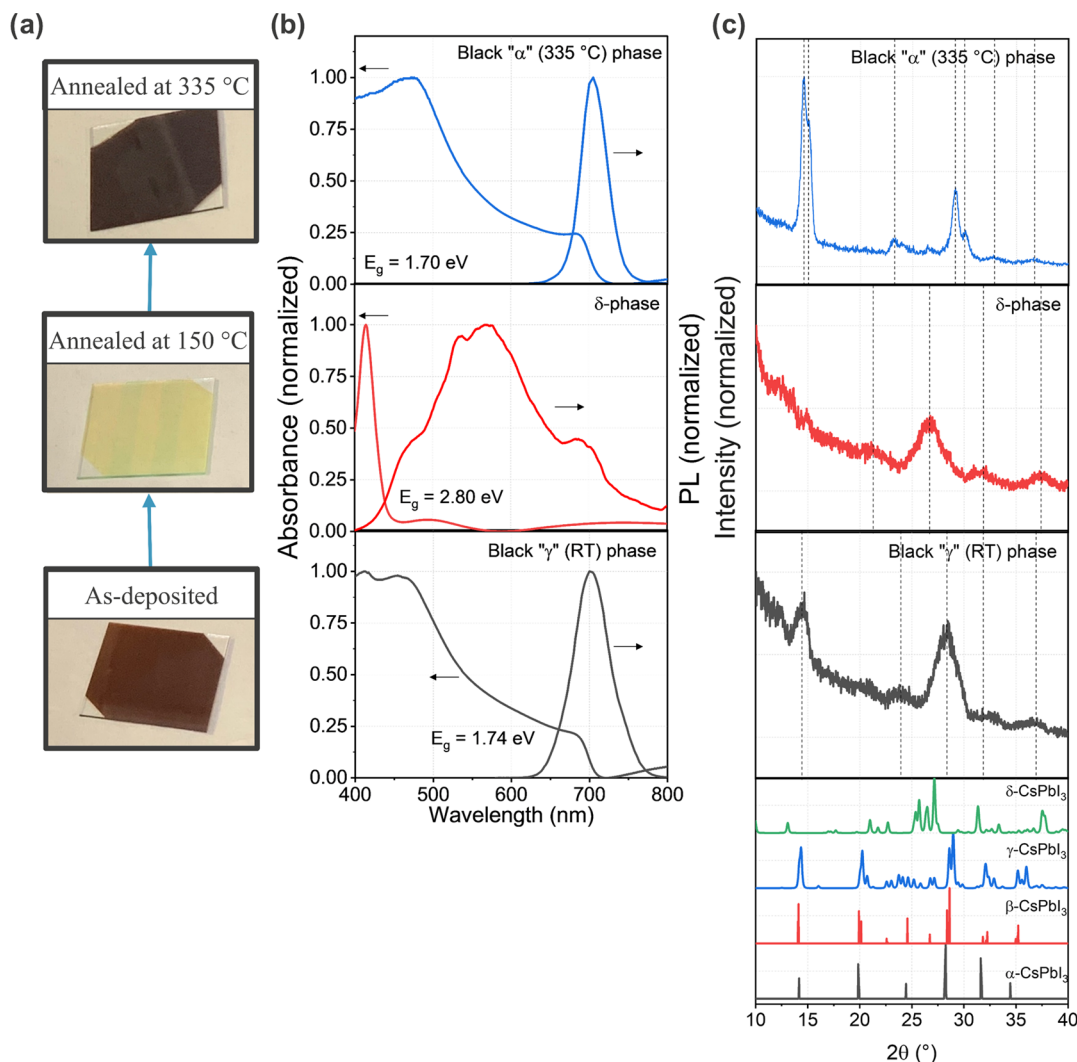
Figure 1. (a) Photographs of 3×3 cm^2 substrates of the transitions of CsPbI$_3$ films: the as-deposited film (bottom) exhibits a dark brown color, which transitions to yellow as the film is annealed at 150 °C (middle); finally, when the film is annealed at 335 °C (top), it exhibits a darker, almost black, color. (b) Corresponding absorbance and photoluminescence spectra for each of the phases: the as-deposited film and the film annealed at 335 °C show very similar absorbance and PL spectrum, while the annealed film at 150 °C has a slightly narrower band gap. The film annealed at 150 °C has a notably larger band gap and a broad-band emission spectrum. (c) Comparison of the X-ray diffraction (XRD) spectra for the three CsPbI$_3$ phases. The as-deposited film has very broad peaks that indicate a nanocrystalline structure and that correspond to the γ-phase. The film annealed at 150 °C also exhibits broad peaks but corresponding to the δ-phase. Finally, the spectrum for the films annealed at 335 °C shows sharper, narrower peaks, indicating a larger crystallite size. The presence of a double peak at ~15° and again at ~28° indicates that this film does not belong completely to the α-phase but to a mix of phases.

moisture.[15−20] Besides the perovskite cubic α-phase, CsPbI$_3$ exists in other phases: an orthorhombic δ-phase (or yellow phase), an orthorhombic (or distorted cubic) γ-phase, and a tetragonal β-phase.[14,18,21−24] Among these, both β- and γ-phases exhibit electronic and optical properties close to those of the α-phase, and many reports refer to them in conjunction, and/or without distinction, as the "black" phase.[24−28] Nevertheless, it is not the black phase but the "yellow" δ-phase that is most stable at normal conditions of temperature and pressure, having a considerably larger band gap (2.8 eV), which makes it unattractive for solar cell or broad-band photodetector applications.[12,24,29] Although the perovskite α-phase can be achieved and maintained at higher temperatures (>300 °C), it quickly transforms to the δ-phase when exposed to moisture or when slowly cooled down (due to the small size of the Cs cation, which cannot support the PbI$_6$ polyhedral frame in the cubic perovskite structure, leading to a low Goldschmidt

tolerance factor),[21,22,30−32] resulting in a different set of challenges, even when this transition is reversible.[7,29,33] However, CsPbI$_3$ can remain in the black phase when stored in nitrogen, if rapidly cooled down after annealing—so-called thermal quenching—as the nonequilibrium process prevents the transition to the yellow phase by introducing stress in the lattice.[8,24] Several efforts have been made to "fix" the black phase and make it stable in air atmosphere, such as introducing stabilizing agents, passivating surfaces, doping with other halides, replacing lead with indium, bismuth, or tin, or reducing the grain size (i.e., nanocrystals and quantum dots),[7,9,13,16,17,22,29,31,34] which results, in many cases, in the black phase consisting of a mix of phases or simply exhibiting the β- or γ-phases, even though it is often reported as the α-phase.[27,35,36] Nevertheless, more work must be done to position CsPbI$_3$-based devices at the level of the MAPbI$_3$-based ones. So far, most of the deposition methods involve

spin coating (SC) of the perovskite, which limits the reproducibility of the devices and their scalability over large areas. The use of organic or polymer stabilizing agents brings back the disadvantages inherent to organic materials, reducing the stability of the devices and limiting their operation in harsh environments.[34] Furthermore, recent device work focuses mainly on the modification of the perovskite layer while using the same organic layers that are used in $MAPbI_3$-based solar cell structures: poly(3,4-ethylenedioxythiophene) polystyrene sulfonate (PEDOT:PSS), 2,2′,7,7′-tetrakis [N,N-di(4-methoxyphenyl)amino]-9,9′-spirobifluorene (spiro-OMe-TAD), poly[bis(4-phenyl)(2,4,6-trimethylphenyl)amine] (PTAA), and poly(3-hexylthiophene) (P3HT) as hole transport layers (HTLs) and [6,6]-phenyl-C_{61}-butyric acid methyl ester (PCBM) or 2,9-dimethyl-4,7-diphenyl-1,10-phenanthroline (BCP) as electron transport layers (ETLs).[3,5,7,37] The application of organic transport layers is limiting the advantages of using an inorganic perovskite. In the case of inorganic transport layers, two main materials have been explored for both $MAPbX_3$ and $CsPbX_3$ devices: mesoporous or compact TiO_2 as an ETL, commonly deposited by spin coating,[3,17,22,30] and NiO as an HTL, mainly deposited by magnetron sputtering or pulsed laser deposition and utilized in inverted devices;[38−40] regardless, the implementation of both TiO_2 and NiO in the same structure is not common. In this paper, we evaluate the deposition of $CsPbI_3$ by thermal evaporation in a co-evaporation approach, offering good thickness control and reproducibility. Post-deposition annealing and fast cool down are subsequently combined to "fix" the black phase in a moisture-free atmosphere.[37] Additionally, we investigate the use of evaporated inorganic transport layers to obtain all-inorganic, all-evaporated devices with solar cell and broad-band, in the whole visible range, photodetector applications. The introduction of all-evaporated layers in a simple structure allows for a better control of the layer thickness, decreasing the number of defects and improving the quality of the interfaces between layers, while increasing the reproducibility of the devices and enabling their large area scalability.[37,39] On the other side, although being all-inorganic, the devices could be operated in harsh environments and at higher temperature ranges with limited degradation, while uniform inorganic contact layers can also act as effective barrier layers to protect the active layer against moisture and oxygen.

2. RESULTS AND DISCUSSION

For the fabrication of the perovskite films, we apply a co-evaporation approach of CsI and PbI_2 as described in Section 4. The as-deposited samples exhibit a dark brown color, which has previously been attributed to the γ-phase; this phase is obtained at low substrate temperatures and is a feature unique to the evaporation technique, for stoichiometric or CsI-rich samples.[8,18,37] Even when the γ-phase (which has also been referred to as the α′-phase) is present at room temperature under a nitrogen atmosphere, it exhibits a slightly larger band gap than the α-phase,[8,12] and it irreversibly transforms to the δ-phase at temperatures higher than 150 °C or when exposed to air and humidity. To obtain the reversible black phase, samples were annealed inside a glovebox in two steps: first, at 150 °C until they transition to the δ-phase and second, at 335 °C to obtain the desired black phase. Afterward, samples were rapidly cooled down by placing them on a metallic surface to fix the black phase at room temperature. This annealing in a temperature range between 310 and 330 °C, followed by a

rapid cool down, has been carried out for previously reported evaporated films, either by co-evaporation[8,41] or by a layer-by-layer approach.[5,37,42] Figure 1a shows the photographs of a film as it goes through the different phases: the as-deposited films (bottom) are brown, transitioning to yellow when they are annealed at 150 °C (middle) and then to a darker, almost black, color (top) when annealed at 335 °C. The absorbance and photoluminescence (PL) spectra for the different phases can be observed in Figure 1b. The as-deposited film and the film annealed at 335 °C exhibit very similar spectra for both absorbance and PL, with the latter having a slightly narrower band gap (1.7 eV, as calculated from the Tauc plot) and a PL emission peak at 706 nm. These values are in agreement with values previously reported in the literature for spin-coated and evaporated black $CsPbI_3$ films.[21,34,37] The difference between the PL emission peak and the band gap value is due to a Stokes shift of ∼47 meV, related to the vibrational relaxation of the lattice, and is in agreement with values reported for $MAPbBr_3$ and $CsPbBr_3$.[43] Films in the yellow phase (annealed at 150 °C) have a considerably larger band gap (2.8 eV) and exhibit a broad-band (400−800 nm) emission spectrum. Absorbance spectrum agrees with values previously reported.[16] There is almost no information about the PL spectrum of the yellow phase, as it is not as interesting for the scientific community as the black phases are; however, a broad-band emission has also been reported.[16,44]

X-ray diffraction (XRD) patterns corresponding to the three different phases observed in the films were also obtained and are shown in Figure 1c. For this, it was important to understand how the films grow on the substrates used for the device fabrication, as results can considerably differ from the growth of films on glass.[45−47] Films were deposited on glass/indium tin oxide (ITO)/NiO substrates and subjected to post-annealing as described above. The XRD spectra are compared with references from the literature; references for α- and β-phases correspond to previous reports that discuss the synthesis and differentiation of the β-phase $CsPbI_3$,[14,26,48] while patterns for both δ- and γ-phases have been obtained from Straus et al.[49] As it can be seen, the as-deposited films (bottom) exhibit two very broad peaks, related to their nanostructured nature and can be mostly assigned to the $CsPbI_3$ γ-phase, as previously reported for as-deposited evaporated films, with the main peak located at ∼28°.[12,18] As the films are annealed at 150 °C, a shift in the main peak toward lower angles can be observed, corresponding to the transition to the δ-phase. The peak is still broad, indicating that there is no considerable change in the crystallite size of the films. This transition also agrees with previous evaporation reports.[12,18] Finally, when the films are annealed at 335 °C, a new transition occurs. In this case, not only the peaks become sharper and narrower, a change in preferential orientation is also present, when compared with as-deposited films. Two double peaks can be observed at around 14.5−15° and then again at 28−30°. These features of double peaks—and a shift of peaks to larger angles due to the stress generated by the fast cool down that the films are subjected to or due to the substrates—complicate the determination of the α-, β-, or γ-phases in annealed films, as all phases share main peaks at similar angles. It can be argued that by rapidly cooling down the films after annealing, a partial transition from the perovskite phase to quasi-perovskite β- or γ-phases occurs and the films are a mix of all of the black phases, something that has been discussed before.[24,37,49] The origin of this mix is
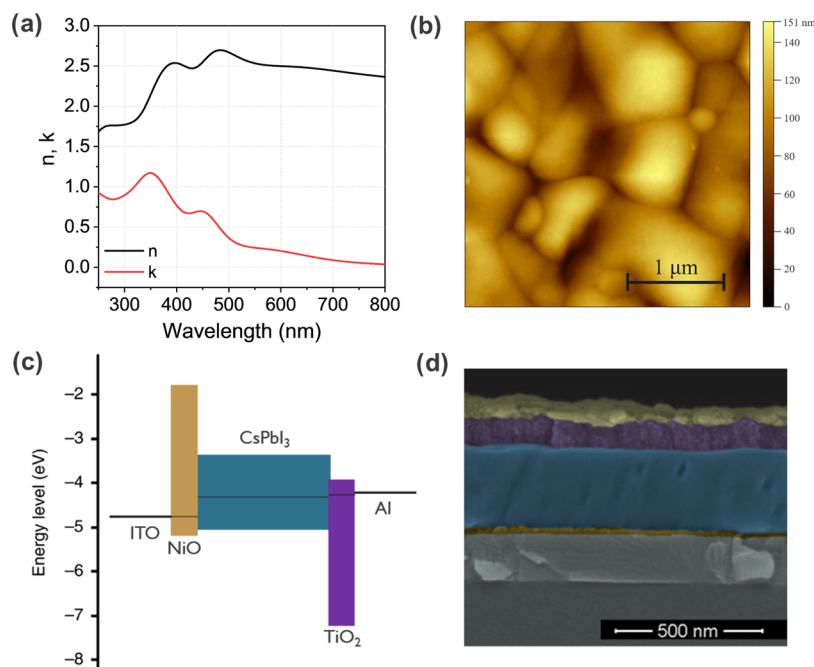
Figure 2. (a) Values of n and k for the black phase of $CsPbI_3$. (b) AFM images showing the roughness of the perovskite films, with an average root-mean-square roughness of 22 nm. (c) Band diagram of the $CsPbI_3$-based device, using NiO and TiO_2 as transport layers. (d) Scanning electron microscopy (SEM) cross section of the device. The interface between the layers is clean and the perovskite is dense and without short circuits.

due to the transition of the α-phase to the other black phases (β- or γ-phases) as it cools down, before converting back to yellow.[14] The crystalline structure of the "fix" black phase then depends on the cooling method (in this case, a fast cooling using a metal surface) and the layers below the perovskite. More importantly, no typical peaks corresponding to the yellow phase were observed. When compared with other black $CsPbI_3$ deposited by co-evaporation, Burwig et al. observed the black phase and determined it to be the α-phase in films deposited on glass and annealed; however, their films also exhibit some peaks which they could not identify as belonging to the α-phase, and their angles seem to be corresponding to the γ-phase. They also observed a shifting in the main peak toward lower angles. This evidence agrees with our findings and is pointing to a mix of phases instead of the α-phase as they have claimed.[12] Hutter et al. deposited $CsPbI_3$ films on quartz, and, after annealing, besides a shifting of the peaks due to the stress while cooling down, peaks corresponding to PbI_2 could also be identified, indicating that they had excess of PbI_2 in their films.[37] It is worth noting that the XRD of the films reported here is for films grown on top of glass/ITO/NiO to represent the films that are used for the devices, and, as mentioned before, we do not observe any peak corresponding to the yellow $CsPbI_3$ phase nor to PbI_2 or CsI precursors.

To determine the thickness of the black $CsPbI_3$ films, variable angle spectroscopic ellipsometry (VASE) measurements were performed, and the values of the refractive index (n) and extinction coefficient (k) were obtained by fitting Ψ and Δ values to the adequate model constructed using the commercially available software CompleteEASE (J.A. Woollam). The resulting values of n and k are shown in Figure 2a. Although there are not many reports in the literature, these values agree with values recently reported by Yan et al.[21] With the determined optical constants and the application of transfer matrix simulations, we optimized the device architecture by targeting maximum light absorption with a

low active layer thickness. The optimum perovskite film thickness was determined to be 260 nm. Atomic force microscopy (AFM) was performed to measure the roughness of the films deposited on glass/ITO/NiO and with a TiO_2 layer on top of the perovskite, to prevent its conversion to the δ-phase during measurements in air. According to the AFM images (Figure 2b), the grains are large in size with an average diameter of 1 μm, which helps decreasing the amount of defects and traps accumulated in the grain boundaries.[39] The average roughness was calculated as ~20 nm, which is a considerable improvement from previously reported evaporated films and closer to the roughness reported for spin-coated films.[8,21,37]

Devices were fabricated using the $CsPbI_3$ layer as the active layer. For this, ITO was used as the bottom electrode, NiO was selected as an HTL, TiO_2 as an ETL, and aluminum as the top contact, as described in Section 4. Both TiO_2 and NiO have been explored for several $MAPbX_3$- and $CsPbX_3$-based devices, although independently and usually not evaporated.[38] In this case, NiO was deposited by reactive magnetron sputtering on top of ITO, controlling the resistivity of the films by controlling the amount of oxygen during deposition. This approach to obtain NiO films has been reported before.[50,51] TiO_2 was deposited by reactive e-beam evaporation with an oxygen partial pressure of 1×10^{-4} mbar, to compensate vacancies created during deposition as previously used for $MAPbI_{3-x}Cl_x$-based solar cells.[52] Figure 2c shows the band diagram of the device. As can be seen, NiO besides working as an HTL offers a high electron affinity working as an electron blocking layer (EBL);[50,53] at the same time, TiO_2 is acting as a hole blocking layer (HBL).[54,55] Using both, NiO and TiO_2, allows us to achieve low leakage current while keeping a simple structure. Figure 2d shows the full device cross section obtained by scanning electron microscopy (SEM). From the image, it is observed that all layers are compact and continuous, with the perovskite having the aimed thickness
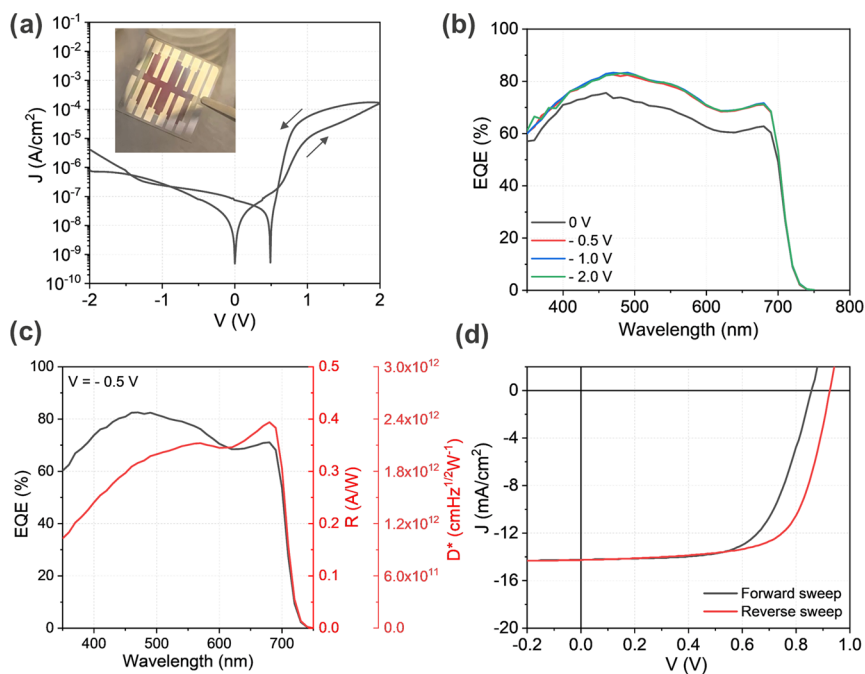
Figure 3. (a) Device $J-V$ curves in the dark for both forward and reverse sweeps. The device exhibits hysteresis, as commonly happens with perovskite-based devices. Inset shows a photograph of a finished sample. (b) EQE vs wavelength for the device when biased at different voltages. Saturation is reached at a negative bias of −0.5 V. (c) EQE, R, and D^* of the device when biased at −0.5 V. (d) Solar cell performance for both forward and reverse sweeps. Efficiency of 7−8% was achieved.

and being dense and without cracks. This is an improvement when compared with spin-coated devices without additives or ligands, where pin holes, defects, or low densities can be found.[33] The image also shows that the deposition of TiO_2 by e-beam does not damage the perovskite below, with a clean interface between layers.

Figure 3a shows the diode $J-V$ curves in the dark, for both forward and reverse sweeps. Low leakage current ($\sim 10^{-7}$ A/cm^2) at low negative voltage (−0.5 V) has been achieved, which is necessary for the photodetector lower detection limit. However, devices exhibit hysteresis, as is common with perovskite-based devices.[56] In addition to low leakage current, high external quantum efficiency (EQE) is also needed for high photodetector and solar cell performances. EQE indicates the probability of generating a charge carrier in the photodetector upon incident light.[34] The EQE spectra (Figure 3b) show high EQE for all visible wavelengths below the perovskite band gap, even at 0 V, and reaching saturation at a negative bias of −0.5 V. This means that no larger negative voltages are needed to obtain a high EQE, and, therefore, the device can perform in photodetector mode at a low negative bias, where the leakage current is low and low light intensities can be detected. The obtained values of EQE are in agreement with values reported in the literature for both spin-coated and evaporated devices.[8,9,17,30]

Besides EQE, for the application of the devices as photodetectors, responsivity R and specific detectivity D^* are important figures of merit. Responsivity shows how efficiently an optical signal is transformed into an electrical signal by the photodetector and is defined as the amount of current that can be produced per watt of incident illumination at a given wavelength (A/W), which is given by[9,19,57]

$$R = \frac{I_{ph}}{P_{opt}} \; (A/W) \tag{1}$$

where I_{ph} is the produced photocurrent and P_{opt} is the optical power. Responsivity is linked to EQE through the following equation[32,57]

$$R = \frac{e}{hc/\lambda} \times EQE \tag{2}$$

where e is the electron charge, h is Planck's constant, c is the speed of light, and λ is the incoming wavelength.

Specific detectivity describes the ability of a device to detect weak signals in the presence of noise and is determined by both the device responsivity and the noise current, or noise equivalent power (NEP), as $D^* = \sqrt{(A\Delta f)}/NEP$. Considering that shot noise is the main contributor to the NEP in the dark and that the contributions of Johnson and flick noise are insignificant, D^* can be defined as[32,57,58]

$$D^* = R/(2eJ_{dark})^{1/2} \; (cm\,Hz^{1/2}/W) \tag{3}$$

where J_{dark} is the dark current density of the device. EQE, R, and D^* are plotted for the device when biased at −0.5 V (Figure 3c). Both R and D^* values are considerably higher than other $CsPbI_3$-based photodetectors, calculated as 0.4 A/W and 2.4×10^{12} cm Hz$^{1/2}$/W (or Jones), respectively, for wavelengths in the 650−680 nm range. These values correspond to the obtained high EQE and imply a good conversion of photons to charge carriers and their collection at the contacts. EQE higher than 100% (gain) is impossible to achieve without the presence of traps that generate a multiplying effect and is less common for a photodiode structure when compared with phototransistors or photoconductors.[57,58]
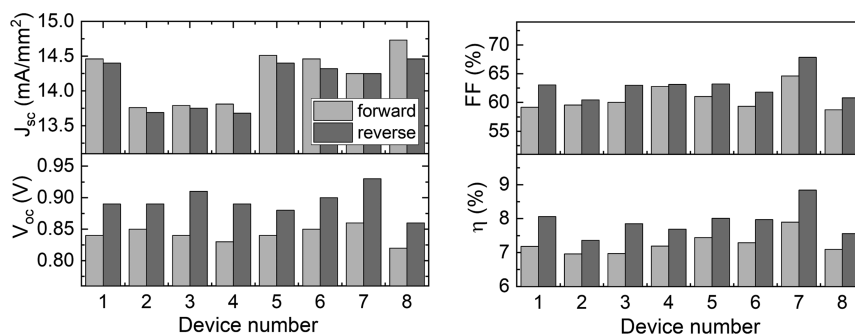
Figure 4. Statistics for several CsPbI$_3$-based solar cells, for both forward and reverse sweeps.
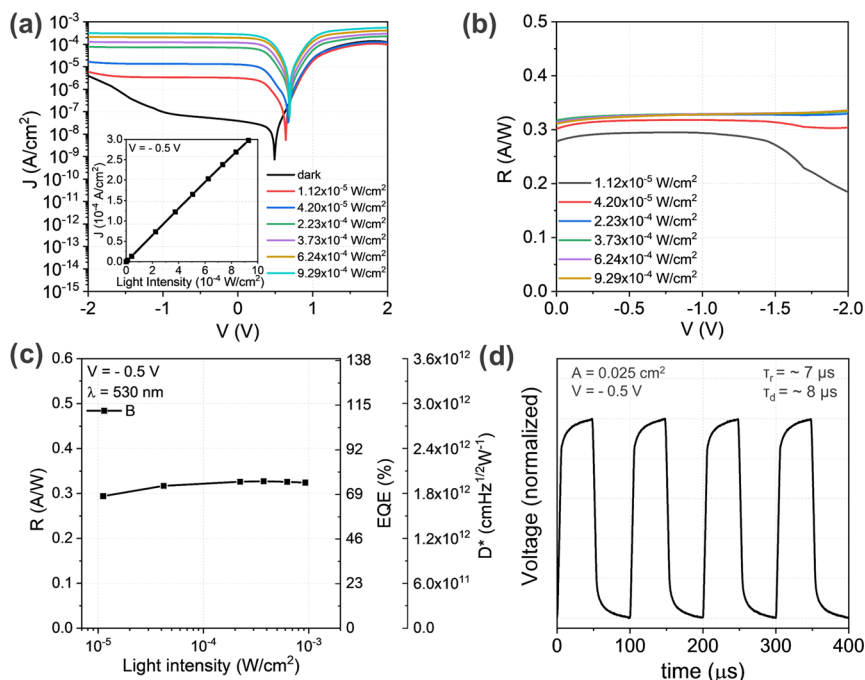
Figure 5. (a) CsPbI$_3$ photodetector performance when illuminated with a 530 nm LED at different light intensities. Inset shows the linear behavior of the current density with the light intensity, exhibiting a constant responsivity at −0.5 V. (b) Responsivity vs voltage curve for different light intensities. Responsivity values are constant in the range of 0 to −1.5 V. (c) Photodetector R, EQE, and D^* values for different light intensities when illuminated with a 530 nm LED and biased at −0.5 V. Devices are well behaved throughout the whole range of light intensities. (d) Time-dependent photoresponse when the device is biased at −0.5 V. Rise and decay time are in the range of 7−8 μs for a size of 0.025 cm^2.

The device performance as a solar cell is shown in Figure 3d. In similarity to the J−V curves in the dark, the J−V curves in light also present normal hysteresis—when fill factor (FF) and/or V_{oc} values are higher for reverse sweep—with devices exhibiting an efficiency of 8.84% for reverse sweep and 7.90% for forward sweep.[56] This difference in the efficiency is due to the difference in the open circuit voltage (V_{oc}) values, measured as 0.93 V and 0.86 V, respectively. CsPbI$_3$-based devices fabricated by spin coating or co-evaporation exhibit the same hysteresis, with higher V_{oc} values for the reverse sweep curves.[8,17] Besides V_{oc}, short-circuit current (J_{sc}) and fill factor (FF) values were obtained as 14.3 mA/cm^2 and 59%, respectively, for forward sweep and 14.3 mA/cm^2 and 68%, respectively, for reverse sweep. Even when J_{sc} values are in agreement with values reported for CsPbI$_3$, they are lower than the values obtained for MAPbI$_3$, which is mostly related to the difference in the band gap of the materials.[8,17,37] Statistics for different devices are shown in Figure 4, for both forward and reverse sweeps. The average efficiency was calculated as 7.3% for forward sweep and 7.9% for reverse sweep, with a standard deviation of 0.3 and 0.4%, respectively. Despite the fact that these efficiencies are lower than efficiencies reported for spin-coated devices using organic transport layers and organic surface-passivating agents or by partially replacing Pb with other elements such as In (10−17%),[17,22,30,31] results agree with spin-coated devices without further treatment (η = 8%, J_{sc} = 16 mA/cm^2, V_{oc} = 0.89 V, FF = 57%)[30] and with devices using an evaporated CsPbI$_3$ but with organic layers (7−9%).[5,8,37,41] Talking about the exhibited hysteresis, this phenomenon has been attributed to the device architecture, the materials used, and even to the test conditions. For example, the use of planar TiO$_2$ when compared with mesoporous TiO$_2$ has been discussed as a source of hysteresis, as mesoporous TiO$_2$ offers a larger contact area with the perovskite, which leads to more efficient electron transfer and separation.[56] Similar hysteresis has been observed when using e-beam-evaporated TiO$_2$ for MAPbI$_{3−x}$Cl$_3$ solar cells.[52] However, the use of mesoporous TiO$_2$ also leads to higher leakage current, which is unwanted for photodetector applications.[3] Another reason for hysteresis might be related

Table 1. Comparison of the Performance of CsPbI$_3$-Based Devices Reported Here with Other CsPbI$_3$-Based Photodetectors Previously Reported in the Literature (PV = CsPbI$_3$)

device	method	structure	J_d (A/cm^2)	R (A/W)	EQE (%)	D^* (cm Hz$^{1/2}$/W)	τ_r/τ_d	ref
Au/PV/Au	SC	MSM				6.29×10^{11}	24/29 ms	13
Au/CsPbI$_2$Br/Au	SC	MSM		~0.05@520 nm		~5.5×10^{11}	90/110 ms	63
FTO/PV/FTO	SC	MSM					100/100 ms	64
Si/SiO$_2$/PV/C8BTBT/Au	DC	photoTFT	~10^{-11} A	~2@−30 V (white light)			seconds	15
Si/SiO$_2$/PV/Au	drop casting	photoTFT	~10^{-9} A@−0.2 V	~0.75@530 nm		~3.5×10^{10}		65
Si/SiO$_2$/MoS$_2$/CsPbI$_{1-x}$Br$_x$/Au	SC	photoTFT	~10^{-11} A	~100@−60 V (532 nm)	10^4	~10^9	0.59/0.32 s	66
ITO/SnO$_2$/PV/Au	SC	photodiode		0.1@550 nm	25@550 nm	1.0×10^{12}	5.7/6.2 μs	34
ITO/ZnO/PV/P3HT/MoO$_3$/Ag	SC	photodiode	10^{-7}@−0.5 V	0.028@550 nm		1.6×10^{12}		9
FTO/TiO$_2$/PV/Spiro-OMeTAD/Ag	SC	photodiode	10^{-7}@−0.8 V	0.09@550 nm		1×10^{13}@0 V		67
ITO/ZnO/PbS/TBAI/PV/Au	SC	photodiode	10^{-7}@−1 V	~2@−1 V (white light)		~4×10^{12}	0.68/0.45 s	68
ITO/NiO/PV/TiO$_2$/Al	evaporation	photodiode	10^{-7}@−0.5 V	0.34@530 nm	80@530 nm	2×10^{12}	7/8 μs	this work

SC = spin coating, DC = dip-coating.

to the presence of traps, leading to nonradiative recombination. In this case, nonradiative recombination losses should be further minimized, by both improving the quality of the perovskite and by passivating the interface between layers.[56] This will also lead to a larger V_{oc} and to achieve higher efficiencies.[29,59] However, the devices reported here show promising results for being all-inorganic, all-evaporated devices based on CsPbI$_3$. More importantly, these devices can be operated as solar cells or photodetectors without any change in the device structure or fabrication.

The application of the devices as photodetectors was further evaluated by obtaining their response to a 530 nm wavelength LED while varying the light intensity (Figure 5a). As expected, the photocurrent of the devices increases as the light intensity increases, with a linear response, indicating a stable responsivity (inset). From these curves, the responsivity of the device to different light intensities and at different voltages was obtained (Figure 5b). Responsivity values are in agreement with the obtained EQE for the 530 nm wavelength. The responsivity of the devices remains fairly constant regardless of the light intensity and the applied negative voltage, which is a good indicator of the quality of the devices. However, responsivity slightly decreases toward low light intensities, explained by traps being filled, although this effect is rather small. The larger decrease of R toward larger negative voltages for low light intensities is linked to the larger leakage current at said values. However, for $V \geq -1.5$ V, the devices are well behaved. Moreover, as the devices exhibit a saturated EQE at −0.5 V, there is no need to bias them at even lower voltages. Figure 5c shows the values of R, EQE, and D^* for the device biased at −0.5 V and under different light intensities. As it can be seen, the device is well behaved throughout the whole range of light intensities, with high values of EQE and R for the 530 nm wavelength. The values of D^* are also high, showing the ability of the device to respond to low light intensities.

Finally, it is important to also determine the speed of the devices. Besides exhibiting high responsivity and detectivity, fast response times broaden the application range. The speed of the devices is determined by their rise (τ_r, 10−90%) and decay time (τ_d, 90−10%).[2] Figure 5d shows the multicycle transient photoresponse of the devices while being illuminated

with a 530 nm wavelength LED at low light intensities. For a device with an active area of 0.025 cm^2, τ_r and τ_d were calculated as 7 and 8 μs, respectively. From τ_r values, the 3 dB cutoff frequency (f_{3dB}) can be calculated. This f_{3dB} corresponds to the input light frequency at which the output signal is 3 dB lower than the signal of the continuous wave modulation[9] and is given by[60,61]

$$f_{3dB} \approx 0.35/\tau_r \; (\text{Hz}) \tag{4}$$

From this, f_{3dB} was calculated as 50 kHz, which is fast enough for imagers applications.[11] However, to obtain faster response and, therefore, larger f_{3dB}, the dimensions of the photodetectors can be further decreased from these large area devices, by reducing the capacitance values of the photodiode and, in result, reducing the RC time constant of the detector.[60,62]

The performance of the photodetectors reported here is comparable with spin-coated MAPbI$_3$-based devices, exhibiting similar leakage current, detectivity, EQE, and responsivity values.[2,39,60] Moreover, the promising performance is also demonstrated when comparing with other CsPbI$_3$-based detectors. Devices based on polymer-wrapped CsPbI$_3$ exhibit a breakdown voltage of −0.4 V, considerably lower responsivity and EQE, with values of 0.1 W/A and 25%, respectively, and similar rise and decay times.[34] CsPbI$_3$ photodetectors based on metal−semiconductor−metal (MSM) interdigitated structures exhibit considerably higher rise and decay time, measured as 24 and 29 ms, respectively.[13] For phototransistors, even when the obtained responsivity is orders of magnitude higher, the required voltage applied at the gate (V_G) goes up to −60 V, and the response time can be in the range of seconds. Furthermore, the devices exhibit gain at low light intensities, which results in a nonconstant responsivity.[15] Comparing with CsPbI$_3$ photodiodes reported by Sim et al., both devices exhibit similar leakage current; however, their devices are 2× thicker than the devices reported here, while their responsivity is 10× smaller and their f_{3dB} about 7× smaller.[9] Table 1 shows a comparison between the devices reported here and other CsPbI$_3$-based photodetectors previously reported. A comparison of different device structures based on the device rise time vs responsivity is

also shown in Figure 6, demonstrating that devices with higher responsivity are also considerably slower, while devices that
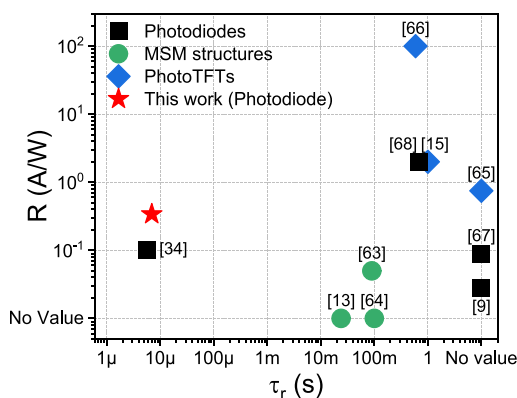
Figure 6. Comparison of the performance, in terms of rise time and responsivity, of the CsPbI$_3$-based photodetector reported here with other CsPbI$_3$-based photodetectors reported in the literature (references are added to each graph point). As it can be seen, the responsivity is higher than most MSM and photodiodes while the rise time is faster than most of the devices previously reported.

exhibit a faster response have lower responsivity. As it can be seen, the devices reported in this work show promising results as photodetectors, with high responsivity, specific detectivity, and fast response.

3. CONCLUSIONS

In summary, we have demonstrated all-inorganic all-vacuum-evaporated CsPbI$_3$ perovskite-based devices and their application as broad-band photodetectors and solar cells. The different layers were deposited by sputtering, thermal, or e-beam evaporation, enabling integration in large area electronics by precise process parameter control and high throughput. Films are dense with a low roughness of ~20 nm, according to AFM images. Devices show low leakage current, ~10^{-7} A/cm^2 at −0.5 V, with EQE higher than 70% over the entire visible range. Additionally, devices show high responsivity, 0.2−0.4 A/W, and high specific detectivity, 1−2 cm Hz$^{1/2}$/W, in the visible-light range. Of special interest for imagers are the high detectivity for low light intensity detection and a constant responsivity over a broad range of light intensities. The speed of these devices was also measured, with a rise and decay time of 7 and 8 μs, respectively, which can be further improved by decreasing the detector area. Benchmarking with already existing CsPbI$_3$ photodetectors exhibits the potential of this fabrication and architecture concept. Finally, the versatility of the exact same devices has been demonstrated by evaluating their performance as solar cells, with efficiencies in the range of 7−8%. Even though this efficiency is lower than CsPbI$_3$-based solar cells that are deposited by spin coating and passivated using organic ligands, it can be further improved by tuning the interfaces between layers. We believe that these full-evaporated CsPbI$_3$-based devices can in the future combine high performance with long-term stability due to their fully inorganic nature.

4. EXPERIMENTAL SECTION

4.1. Perovskite Deposition. CsPbI$_3$ thin films were deposited by thermal evaporation from the co-evaporation of CsI (abcr, ultra-dry) and PbI$_2$ (TCI Chemicals) precursors, calibrating the deposition rate

of each precursor based on a 1:1 CsI to PbI$_2$ molar ratio for stoichiometric films. The precursor deposition rates were calibrated by ellipsometry (RC2, J.A. Woollam). The evaporation system was fabricated in-house, with a source to substrate distance of ~30 cm and shutters for both sources and substrate. During deposition, the substrate was fixed in one position and heated up to 60 °C. After deposition, brown as-deposited samples were obtained, linked to the γ-phase. To obtain and fix the cubic α-phase, samples were annealed inside a glovebox first at 150 °C and then at 335 °C until they transition to yellow and then to black, respectively. After that, samples were cooled down rapidly by placing them on a metallic surface to fix the black phase.

4.2. Device Fabrication. For the devices, 3 × 3 cm^2 glass substrates with prepatterned ITO strips (15 Ω, Colorado Concept Coatings) were cleaned in an ultrasonic bath using Extran, water, acetone, and isopropanol, successively, and dried out using a nitrogen gun. As an HTL, 15 nm thick NiO films were deposited on top of the substrates by reactive sputtering in a Nebula system from Angstrom Engineering Inc., with a metallic nickel target and introducing oxygen during deposition. Samples were then annealed at 300 °C in air for 30 min and annealed again for 30 min at 150 °C inside a glovebox to remove any adsorbed humidity before the perovskite deposition. Afterward, 260 nm thick CsPbI$_3$ films were deposited and annealed as described above. As an ETL, 85 nm thick TiO$_2$ films were deposited by e-beam evaporation in a high vacuum system (Angstrom Engineering Inc.), introducing oxygen during deposition to compensate oxygen vacancies and keeping the deposition rate at 0.3 Å/s to prevent damage to the perovskite film. Finally, 80 nm thick Al contacts were deposited by thermal evaporation and using a shadow mask, keeping a low deposition rate of 0.3 Å/s. After the perovskite deposition, devices were always kept under a nitrogen atmosphere to prevent the perovskite conversion to the yellow phase when exposed to air and humidity.

4.3. Device Characterization. To characterize the perovskite films, absorbance, ellipsometry, and PL measurements were performed in air to obtain the band gap, absorption spectra, refractive index and extinction coefficient, thickness, and PL spectra. Absorbance spectra were obtained using a Shimadzu UV1601 spectrophotometer. Ellipsometry measurements were performed in a Woollam RC2 ellipsometer, and PL spectra for both films exhibiting black phases were performed using a Hamamatsu Quantaurus-Tau Fluorescence lifetime spectrometer and using a green (530 nm) excitation laser. Because the Hamamatsu system was not equipped with a laser with shorter wavelength, to obtain the PL spectrum for the yellow CsPbI$_3$ phase (with a band gap of 2.8 eV) a different setup was used. In this case, the PL spectrum was captured by applying 355 nm pump light from a CryLaS FTSS 355−300 laser onto a spot of 600 μm diameter. The laser was pulsed at a rate of 20 Hz and was attenuated to an energy of 62 μJ/pulse. The resultant PL spectrum was captured by sending this light into a SpectraPro HRS-500 spectrograph (Princeton Instruments). To obtain the XRD patterns, measurements of the as-deposited films, films annealed at 150 °C, and films annealed at 335 °C were recorded with a Malvern PANalytical Empyrean diffractometer in reflection mode, using a PIXcel3D solid-state detector and a Cu anode (Cu Kα$_1$: 1.5406 Å; Cu Kα$_2$: 1.5444 Å). The measurements were performed in a 2θ range between 10 and 40°, with a step size of 0.026° at 200 s/step, in a nitrogen atmosphere and at room temperature. AFM images were obtained using a Bruker Dimension Edge system to evaluate the roughness of the films; the measurements were carried out in air, using TiO$_2$ as a capping layer, to prevent the perovskite transition during the measurement. SEM images were obtained using an FEI Nova 200 system to evaluate the cross section of the full devices, and images were artificially colored for easier identification of the layers.

For the electrical and optical characterization of the devices, all measurements were carried out in a nitrogen atmosphere. J−V curves in the dark and under illumination were obtained by measuring the devices using a probe station in a glovebox connected to an Agilent 4156C Semiconductor Parameter Analyzer. To obtain the response of the devices under different light intensities, an M530L2 green (530

nm) LED from Thorlabs was used at ∼20 cm from the device and varying the light intensity with a Thorlabs DC2200 LED driver. The light intensity was calibrated using a Si photodiode. The performance of the device as a solar cell was evaluated using an Abet solar simulator under 100 mW/cm^2 (1 sun) simulated AM 1.5G illumination. For the rise and decay time, devices were encapsulated to be measured in air. The devices were biased at −0.5 V and illuminated with an M530L2 green (530 nm) LED from Thorlabs, 5 cm from the device, and controlled by the Thorlabs DC2200 LED driver. In this case, a light intensity of 30%, a frequency of 10 kHz, and a 50:50 duty cycle were used. The output signal was converted to voltage and amplified using a Femto DHPCA-100 variable gain high-speed current amplifier and collected using a Keysight DSO6102A oscilloscope. EQE measurements were performed using a Bentham PV300 spectral response system, with a xenon/quartz halogen lamp and a Bentham TMc300 single monochromator. Measurements were calibrated using a Si photodiode.

■ AUTHOR INFORMATION

Corresponding Author

Maria Isabel Pintor Monroy − *imec, 3001 Leuven, Belgium; Department of Electrical Engineering (ESAT), KU Leuven, 3001 Leuven, Belgium;* ⊙ orcid.org/0000-0003-0403-602X; Email: isabel.pintormonroy@imec.be

Authors

Iakov Goldberg − *imec, 3001 Leuven, Belgium; Department of Electrical Engineering (ESAT), KU Leuven, 3001 Leuven, Belgium*

Karim Elkhouly − *imec, 3001 Leuven, Belgium; Department of Electrical Engineering (ESAT), KU Leuven, 3001 Leuven, Belgium*

Epimitheas Georgitzikis − *imec, 3001 Leuven, Belgium;* ⊙ orcid.org/0000-0001-5972-8328

Lotte Clinckemalie − *Department of Chemistry, Faculty of Sciences, KU Leuven, 3001 Leuven, Belgium*

Guillaume Croes − *imec, 3001 Leuven, Belgium; Department of Electrical Engineering (ESAT), KU Leuven, 3001 Leuven, Belgium*

Nirav Annavarapu − *imec, 3001 Leuven, Belgium; Department of Electrical Engineering (ESAT), KU Leuven, 3001 Leuven, Belgium*

Weiming Qiu − *imec, 3001 Leuven, Belgium; Department of Chemistry, Faculty of Sciences, KU Leuven, 3001 Leuven, Belgium*

Elke Debroye − *Department of Chemistry, Faculty of Sciences, KU Leuven, 3001 Leuven, Belgium;* ⊙ orcid.org/0000-0003-1087-4759

Yinghuan Kuang − *imec, Partner in Solliance and Energyville, Thin Film PV, 3600 Genk, Belgium*

Maarten B. J. Roeffaers − *cMACS, Department of Microbial and Molecular Systems, KU Leuven, 3001 Leuven, Belgium*

Johan Hofkens − *Department of Chemistry, Faculty of Sciences, KU Leuven, 3001 Leuven, Belgium; Max Planck Institute for Polymer Research, 55128 Mainz, Germany;* ⊙ orcid.org/0000-0002-9101-0567

Robert Gehlhaar − *imec, 3001 Leuven, Belgium*

Jan Genoe − *imec, 3001 Leuven, Belgium; Department of Electrical Engineering (ESAT), KU Leuven, 3001 Leuven, Belgium*

Complete contact information is available at:
https://pubs.acs.org/10.1021/acsaelm.1c00252

Author Contributions

The manuscript was written through contributions of all authors. All authors have given approval to the final version of the manuscript.

Notes

The authors declare no competing financial interest.

■ REFERENCES

(1) Mei, F.; Sun, D.; Mei, S.; Feng, J.; Zhou, Y.; Xu, J.; Xiao, X. Recent Progress in Perovskite-Based Photodetectors: The Design of Materials and Structures. *Adv. Phys.: X* **2019**, *4*, No. 1592709.

(2) Zhao, Y.; Li, C.; Shen, L. Recent Research Process on Perovskite Photodetectors: A Review for Photodetector—Materials, Physics, and Applications. *Chin. Phys. B* **2018**, *27*, No. 127806.

(3) Zhang, C.; Kuang, D.; Wu, W. A Review of Diverse Halide Perovskite Morphologies for Efficient Optoelectronic Applications. *Small Methods* **2020**, *4*, No. 1900662.

(4) Stylianakis, M.; Maksudov, T.; Panagiotopoulos, A.; Kakavelakis, G.; Petridis, K. Inorganic and Hybrid Perovskite Based Laser Devices: A Review. *Materials* **2019**, *12*, No. 859.

(5) Kottokkaran, R.; Gaonkar, H. A.; Bagheri, B.; Dalal, V. L. Efficient P-i-n Inorganic CsPbI$_3$ Perovskite Solar Cell Deposited Using Layer-by-Layer Vacuum Deposition. *J. Vac. Sci. Technol., A* **2018**, *36*, No. 041201.

(6) Hamada, K.; Yonezawa, K.; Yamamoto, K.; Taima, T.; Hayase, S.; Ooyagi, N.; Yamamoto, Y.; Ohdaira, K. Vacuum Deposition of CsPbI$_3$ Layers on Textured Si for Perovskite/Si Tandem Solar Cells. *Jpn. J. Appl. Phys.* **2019**, *58*, No. SBBF06.

(7) Ahmad, W.; Khan, J.; Niu, G.; Tang, J. Inorganic CsPbI$_3$ Perovskite-Based Solar Cells: A Choice for a Tandem Device. *Sol. RRL* **2017**, *1*, No. 1700048.

(8) Frolova, L. A.; Anokhin, D. V.; Piryazev, A. A.; Luchkin, S. Y.; Dremova, N. N.; Stevenson, K. J.; Troshin, P. A. Highly Efficient All-Inorganic Planar Heterojunction Perovskite Solar Cells Produced by Thermal Coevaporation of CsI and PbI$_2$. *J. Phys. Chem. Lett.* **2017**, *8*, 67−72.

(9) Sim, K. M.; Swarnkar, A.; Nag, A.; Chung, D. S. Phase Stabilized α-CsPbI$_3$ Perovskite Nanocrystals for Photodiode Applications. *Laser Photonics Rev.* **2018**, *12*, No. 1700209.

(10) Johnston, M. B. Colour-Selective Photodiodes. *Nat. Photonics* **2015**, *9*, 634−636.

(11) Lin, Q.; Armin, A.; Lyons, D. M.; Burn, P. L.; Meredith, P. Low Noise, IR-Blind Organohalide Perovskite Photodiodes for Visible Light Detection and Imaging. *Adv. Mater.* **2015**, *27*, 2060−2064.

(12) Burwig, T.; Fränzel, W.; Pistor, P. Crystal Phases and Thermal Stability of Co-Evaporated CsPbX$_3$ (X = I, Br) Thin Films. *J. Phys. Chem. Lett.* **2018**, *9*, 4808−4813.

(13) Ramasamy, P.; Lim, D.-H.; Kim, B.; Lee, S.-H.; Lee, M.-S.; Lee, J.-S. All-Inorganic Cesium Lead Halide Perovskite Nanocrystals for Photodetector Applications. *Chem. Commun.* **2016**, *52*, 2067–2070.

(14) Marronnier, A.; Roma, G.; Boyer-Richard, S.; Pedessau, L.; Jancu, J.-M.; Bonnassieux, Y.; Katan, C.; Stoumpos, C. C.; Kanatzidis, M. G.; Even, J. Anharmonicity and Disorder in the Black Phases of Cesium Lead Iodide Used for Stable Inorganic Perovskite Solar Cells. *ACS Nano* **2018**, *12*, 3477–3486.

(15) Chen, Y.; Wu, X.; Chu, Y.; Zhou, J.; Zhou, B.; Huang, J. Hybrid Field-Effect Transistors and Photodetectors Based on Organic Semiconductor and CsPbI3 Perovskite Nanorods Bilayer Structure. *Nano-Micro Lett.* **2018**, *10*, No. 57.

(16) Waleed, A.; Tavakoli, M. M.; Gu, L.; Hussain, S.; Zhang, D.; Poddar, S.; Wang, Z.; Zhang, R.; Fan, Z. All Inorganic Cesium Lead Iodide Perovskite Nanowires with Stabilized Cubic Phase at Room Temperature and Nanowire Array-Based Photodetectors. *Nano Lett.* **2017**, *17*, 4951–4957.

(17) Li, B.; Zhang, Y.; Fu, L.; Yu, T.; Zhou, S.; Zhang, L.; Yin, L. Surface Passivation Engineering Strategy to Fully-Inorganic Cubic CsPbI3 Perovskites for High-Performance Solar Cells. *Nat. Commun.* **2018**, *9*, No. 1076.

(18) Becker, P.; Márquez, J. A.; Just, J.; Al-Ashouri, A.; Hages, C.; Hempel, H.; Jošt, M.; Albrecht, S.; Frahm, R.; Unold, T. Low Temperature Synthesis of Stable Γ-CsPbI$_3$ Perovskite Layers for Solar Cells Obtained by High Throughput Experimentation. *Adv. Energy Mater.* **2019**, *9*, No. 1900555.

(19) Yang, T.; Li, F.; Zheng, R. Recent Progress on Cesium Lead Halide Perovskites for Photodetection Applications. *ACS Appl. Electron. Mater.* **2019**, *1*, 1348–1366.

(20) Zhang, H.; Debroye, E.; Steele, J.; Roeffaers, M. B. J.; Hofkens, J.; Wang, H. I.; Bonn, M. Highly Mobile Large Polarons in Black Phase CsPbI$_3$. *ACS Energy Lett.* **2021**, *6*, 568–573.

(21) Yan, W.; Guo, Y.; Beri, D.; Dottermusch, S.; Chen, H.; Richards, B. S. Experimental Determination of Complex Optical Constants of Air-Stable Inorganic CsPbI$_3$ Perovskite Thin Films. *Phys. Status Solidi RRL* **2020**, *14*, No. 2000070.

(22) Li, Z.; Zhou, F.; Wang, Q.; Ding, L.; Jin, Z. Approaches for Thermodynamically Stabilized CsPbI3 Solar Cells. *Nano Energy* **2020**, *71*, No. 104634.

(23) Sutton, R. J.; Filip, M. R.; Haghighirad, A. A.; Sakai, N.; Wenger, B.; Giustino, F.; Snaith, H. J. Cubic or Orthorhombic? Revealing the Crystal Structure of Metastable Black-Phase CsPbI$_3$ by Theory and Experiment. *ACS Energy Lett.* **2018**, *3*, 1787–1794.

(24) Steele, J. A.; Jin, H.; Dovgaliuk, I.; Berger, R. F.; Braeckevelt, T.; Yuan, H.; Martin, C.; Solano, E.; Lejaeghere, K.; Rogge, S. M. J.; Notebaert, C.; Vandezande, W.; Janssen, K. P. F.; Goderis, B.; Debroye, E.; Wang, Y.-K.; Dong, Y.; Ma, D.; Saidaminov, M.; Tan, H.; Lu, Z.; Dyadkin, V.; Chernyshov, D.; Van Speybroeck, V.; Sargent, E. H.; Hofkens, J.; Roeffaers, M. B. J. Thermal Unequilibrium of Strained Black CsPbI$_3$ Thin Films. *Science* **2019**, *365*, 679–684.

(25) Zhao, H.; Xu, J.; Zhou, S.; Li, Z.; Zhang, B.; Xia, X.; Liu, X.; Dai, S.; Yao, J. Preparation of Tortuous 3D Γ-CsPbI$_3$ Films at Low Temperature by CaI$_2$ as Dopant for Highly Efficient Perovskite Solar Cells. *Adv. Funct. Mater.* **2019**, No. 1808986.

(26) Wang, K.; Tian, Q.; Zhao, G.; Wen, J.; Huang, J.; Gao, C.; Xu, Z.; Liu, Y.; Liang, L.; Meng, L.; Zhang, L.; Liu, Z.; Jin, Z.; Olthof, S.; Liu, S. Beach-Chair-Shaped Energy Band Alignment for High-Performance β-CsPbI3 Solar Cells. *Cell Rep. Phys. Sci.* **2020**, *1*, No. 100180.

(27) Shen, Q.; Ripolles, T. S.; Even, J.; Ogomi, Y.; Nishinaka, K.; Izuishi, T.; Nakazawa, N.; Zhang, Y.; Ding, C.; Liu, F.; Toyoda, T.; Yoshino, K.; Minemoto, T.; Katayama, K.; Hayase, S. Slow Hot Carrier Cooling in Cesium Lead Iodide Perovskites. *Appl. Phys. Lett.* **2017**, *111*, No. 153903.

(28) Chang, X.; Fang, J.; Fan, Y.; Luo, T.; Su, H.; Zhang, Y.; Lu, J.; Tsetseris, L.; Anthopoulos, T. D.; Liu, S.; Zhao, K. Printable CsPbI$_3$ Perovskite Solar Cells with PCE of 19% via an Additive Strategy. *Adv. Mater.* **2020**, *32*, No. 2001243.

(29) Ho-Baillie, A.; Zhang, M.; Lau, C. F. J.; Ma, F.-J.; Huang, S. Untapped Potentials of Inorganic Metal Halide Perovskite Solar Cells. *Joule* **2019**, *3*, 938–955.

(30) Hu, Y.; Bai, F.; Liu, X.; Ji, Q.; Miao, X.; Qiu, T.; Zhang, S. Bismuth Incorporation Stabilized α-CsPbI$_3$ for Fully Inorganic Perovskite Solar Cells. *ACS Energy Lett.* **2017**, *2*, 2219–2227.

(31) Li, X.; Wang, K.; Lgbari, F.; Dong, C.; Yang, W.; Ma, C.; Ma, H.; Wang, Z.-K.; Liao, L.-S. Indium Doped CsPbI3 Films for Inorganic Perovskite Solar Cells with Efficiency Exceeding 17%. *Nano Res.* **2020**, *13*, 2203–2208.

(32) Wang, H.; Kim, D. H. Perovskite-Based Photodetectors: Materials and Devices. *Chem. Soc. Rev.* **2017**, *46*, 5204–5236.

(33) Liu, C.; Yang, Y.; Xia, X.; Ding, Y.; Arain, Z.; An, S.; Liu, X.; Cristina, R. C.; Dai, S.; Nazeeruddin, M. K. Soft Template-Controlled Growth of High-Quality CsPbI$_3$ Films for Efficient and Stable Solar Cells. *Adv. Energy Mater.* **2020**, *10*, No. 1903751.

(34) Bansode, U.; Rahman, A.; Ogale, S. Low-Temperature Processing of Optimally Polymer-Wrapped α-CsPbI$_3$ for Self-Powered Flexible Photo-Detector Application. *J. Mater. Chem. C* **2019**, *7*, 6986–6996.

(35) Eperon, G. E.; Paternò, G. M.; Sutton, R. J.; Zampetti, A.; Haghighirad, A. A.; Cacialli, F.; Snaith, H. J. Inorganic Caesium Lead Iodide Perovskite Solar Cells. *J. Mater. Chem. A* **2015**, *3*, 19688–19695.

(36) Haque, F.; Wright, M.; Mahmud, M. A.; Yi, H.; Wang, D.; Duan, L.; Xu, C.; Upama, M. B.; Uddin, A. Effects of Hydroiodic Acid Concentration on the Properties of CsPbI$_3$ Perovskite Solar Cells. *ACS Omega* **2018**, *3*, 11937–11944.

(37) Hutter, E. M.; Sutton, R. J.; Chandrashekar, S.; Abdi-Jalebi, M.; Stranks, S. D.; Snaith, H. J.; Savenije, T. J. Vapour-Deposited Cesium Lead Iodide Perovskites: Microsecond Charge Carrier Lifetimes and Enhanced Photovoltaic Performance. *ACS Energy Lett.* **2017**, *2*, 1901–1908.

(38) Higgins, M.; Reyes-Banda, M. G.; Martínez-Falomir, G. G.; Bouanani, L. E.; Murillo, B.; Chavez-Urbiola, I. R.; Pintor-Monroy, M. I.; Ely, F.; Mathew, X.; Quevedo-Lopez, M. A. Solvent-Free and Large Area Compatible Deposition of Methylammonium Lead Bromide Perovskite by Close Space Sublimation and Its Application in PIN Diodes. *Thin Solid Films* **2019**, *692*, No. 137585.

(39) Dong, Y.; Zou, Y.; Song, J.; Song, X.; Zeng, H. Recent Progress of Metal Halide Perovskite Photodetectors. *J. Mater. Chem. C* **2017**, *5*, 11369–11394.

(40) Shan, Q.; Li, J.; Song, J.; Zou, Y.; Xu, L.; Xue, J.; Dong, Y.; Huo, C.; Chen, J.; Han, B.; Zeng, H. All-Inorganic Quantum-Dot Light-Emitting Diodes Based on Perovskite Emitters with Low Turn-on Voltage and High Humidity Stability. *J. Mater. Chem. C* **2017**, *5*, 4565–4570.

(41) Chen, C.-Y.; Lin, H.-Y.; Chiang, K.-M.; Tsai, W.-L.; Huang, Y.-C.; Tsao, C.-S.; Lin, H.-W. All-Vacuum-Deposited Stoichiometrically Balanced Inorganic Cesium Lead Halide Perovskite Solar Cells with Stabilized Efficiency Exceeding 11%. *Adv. Mater.* **2017**, *29*, No. 1605290.

(42) Yonezawa, K.; Yamamoto, K.; Shahiduzzaman, M.; Furumoto, Y.; Hamada, K.; Ripolles, T. S.; Karakawa, M.; Kuwabara, T.; Takahashi, K.; Hayase, S.; Taima, T. Annealing Effects on CsPbI$_3$-Based Planar Heterojunction Perovskite Solar Cells Formed by Vacuum Deposition Method. *Jpn. J. Appl. Phys.* **2017**, *56*, No. 04CS11.

(43) Guo, Y.; Yaffe, O.; Hull, T. D.; Owen, J. S.; Reichman, D. R.; Brus, L. E. Dynamic Emission Stokes Shift and Liquid-like Dielectric Solvation of Band Edge Carriers in Lead-Halide Perovskites. *Nat. Commun.* **2019**, *10*, No. 1175.

(44) Chen, Z.; Dong, L.; Tang, H.; Yu, Y.; Ye, L.; Zang, J. Direct Synthesis of Cubic Phase CsPbI$_3$ Nanowires. *CrystEngComm* **2019**, *21*, 1389–1396.

(45) Lu, Y.; Han, Q.; Zhao, Y.; Yang, C.; Li, Y.; Liu, X. Substrate-Dependent Growth of CH$_3$NH$_3$PbI$_3$ Films Deposited by Vacuum Evaporation. *J. Phys.: Conf. Ser.* **2020**, *1637*, No. 012080.

(46) Deng, Y.-H. Substrate Engineering in the Growth of Perovskite Crystals. 2020, arXiv:2010.04422. arXiv.org e-Print archive. https://arxiv.org/abs/2010.04422.

(47) Olthof, S.; Meerholz, K. Substrate-Dependent Electronic Structure and Film Formation of MAPbI3 Perovskites. *Sci. Rep.* **2017**, *7*, No. 40267.

(48) Wang, Y.; Dar, M. I.; Ono, L. K.; Zhang, T.; Kan, M.; Li, Y.; Zhang, L.; Wang, X.; Yang, Y.; Gao, X.; Qi, Y.; Grätzel, M.; Zhao, Y. Thermodynamically Stabilized β-CsPbI$_3$ −Based Perovskite Solar Cells with Efficiencies>18%. *Science* **2019**, *365*, 591−595.

(49) Straus, D. B.; Guo, S.; Cava, R. J. Kinetically Stable Single Crystals of Perovskite-Phase CsPbI$_3$. *J. Am. Chem. Soc.* **2019**, *141*, 11435−11439.

(50) Pintor-Monroy, M. I.; Murillo-Borjas, B. L.; Catalano, M.; Quevedo-Lopez, M. A. Controlling Carrier Type and Concentration in NiO Films To Enable *in Situ* PN Homojunctions. *ACS Appl. Mater. Interfaces* **2019**, *11*, 27048−27056.

(51) Park, J.-W.; Park, J.-W.; Jung, K.; Yang, M. K.; Lee, J.-K. Influence of Oxygen Content on Electrical Properties of NiO Films Grown by Rf Reactive Sputtering for Resistive Random-Access Memory Applications. *J. Vac. Sci. Technol., B: Microelectron. Nanometer Struct.—Process., Meas., Phenom.* **2006**, *24*, 2205.

(52) Qiu, W.; Paetzold, U. W.; Gehlhaar, R.; Smirnov, V.; Boyen, H.-G.; Tait, J. G.; Conings, B.; Zhang, W.; Nielsen, C. B.; McCulloch, I.; Froyen, L.; Heremans, P.; Cheyns, D. An Electron Beam Evaporated TiO$_2$ Layer for High Efficiency Planar Perovskite Solar Cells on Flexible Polyethylene Terephthalate Substrates. *J. Mater. Chem. A* **2015**, *3*, 22824−22829.

(53) Pintor-Monroy, M. I.; Barrera, D.; Murillo-Borjas, B. L.; Ochoa-Estrella, F. J.; Hsu, J. W. P.; Quevedo-Lopez, M. A. Tunable Electrical and Optical Properties of Nickel Oxide (NiO$_x$) Thin Films for Fully Transparent NiO$_x$ −Ga$_2$O$_3$ p−n Junction Diodes. *ACS Appl. Mater. Interfaces* **2018**, *10*, 38159−38165.

(54) Yu, I.-S.; Wang, Y.-W.; Cheng, H.-E.; Yang, Z.-P.; Lin, C.-T. Surface Passivation and Antireflection Behavior of ALD TiO2 on N-Type Silicon for Solar Cells. *Int. J. Photoenergy* **2013**, *2013*, No. 431614.

(55) Marques, F. C.; Jasieniak, J. J. Ionization Potential and Electron Attenuation Length of Titanium Dioxide Deposited by Atomic Layer Deposition Determined by Photoelectron Spectroscopy in Air. *Appl. Surf. Sci.* **2017**, *422*, 504−508.

(56) Liu, P.; Wang, W.; Liu, S.; Yang, H.; Shao, Z. Fundamental Understanding of Photocurrent Hysteresis in Perovskite Solar Cells. *Adv. Energy Mater.* **2019**, *9*, No. 1803017.

(57) Baeg, K.-J.; Binda, M.; Natali, D.; Caironi, M.; Noh, Y.-Y. Organic Light Detectors: Photodiodes and Phototransistors. *Adv. Mater.* **2013**, *25*, 4267−4295.

(58) Pintor-Monroy, M. I.; Murillo-Borjas, B. L.; Quevedo-Lopez, M. A. Nanocrystalline and Polycrystalline β-Ga$_2$O$_3$ Thin Films for Deep Ultraviolet Detectors. *ACS Appl. Electron. Mater.* **2020**, *2*, 3358−3365.

(59) Luo, D.; Su, R.; Zhang, W.; Gong, Q.; Zhu, R. Minimizing Non-Radiative Recombination Losses in Perovskite Solar Cells. *Nat. Rev. Mater.* **2020**, *5*, 44−60.

(60) Fang, Y.; Huang, J. Resolving Weak Light of Sub-Picowatt per Square Centimeter by Hybrid Perovskite Photodetectors Enabled by Noise Reduction. *Adv. Mater.* **2015**, *27*, 2804−2810.

(61) Tong, G.; Li, H.; Li, D.; Zhu, Z.; Xu, E.; Li, G.; Yu, L.; Xu, J.; Jiang, Y. Dual-Phase CsPbBr$_3$ -CsPb$_2$Br$_5$ Perovskite Thin Films via Vapor Deposition for High-Performance Rigid and Flexible Photodetectors. *Small* **2018**, *14*, No. 1702523.

(62) Goushcha, A. O.; Tabbert, B. On Response Time of Semiconductor Photodiodes. *Opt. Eng.* **2017**, *56*, No. 097101.

(63) Liu, Z.; Li, H.; Qin, C.; Zhang, T.; Gu, Y.; Chen, H.; Zheng, H.; Li, S. Solution-Processed Inorganic Perovskite Flexible Photodetectors with High Performance. *Nanoscale Res. Lett.* **2019**, *14*, No. 284.

(64) Liang, J.; Wang, C.; Zhao, P.; Lu, Z.; Ma, Y.; Xu, Z.; Wang, Y.; Zhu, H.; Hu, Y.; Zhu, G.; Ma, L.; Chen, T.; Tie, Z.; Liu, J.; Jin, Z. Solution Synthesis and Phase Control of Inorganic Perovskites for High-Performance Optoelectronic Devices. *Nanoscale* **2017**, *9*, 11841−11845.

(65) Zhou, Y.; Luo, J.; Zhao, Y.; Ge, C.; Wang, C.; Gao, L.; Zhang, C.; Hu, M.; Niu, G.; Tang, J. Flexible Linearly Polarized Photodetectors Based on All-Inorganic Perovskite CsPbI$_3$ Nanowires. *Adv. Opt. Mater.* **2018**, *6*, No. 1800679.

(66) Wu, H.; Si, H.; Zhang, Z.; Kang, Z.; Wu, P.; Zhou, L.; Zhang, S.; Zhang, Z.; Liao, Q.; Zhang, Y. All-Inorganic Perovskite Quantum Dot-Monolayer MoS$_2$ Mixed-Dimensional van Der Waals Heterostructure for Ultrasensitive Photodetector. *Adv. Sci.* **2018**, *5*, No. 1801219.

(67) Bi, C.; Kershaw, S. V.; Rogach, A. L.; Tian, J. Improved Stability and Photodetector Performance of CsPbI$_3$ Perovskite Quantum Dots by Ligand Exchange with Aminoethanethiol. *Adv. Funct. Mater.* **2019**, *29*, No. 1902446.

(68) Saleem, M. I.; Yang, S.; Batool, A.; Sulaman, M.; Veeramalai, C. P.; Jiang, Y.; Tang, Y.; Cui, Y.; Tang, L.; Zou, B. CsPbI3 Nanorods as the Interfacial Layer for High-Performance, All-Solution-Processed Self-Powered Photodetectors. *J. Mater. Sci. Technol.* **2020**, 196−204.